Journal of Materials Chemistry A

ROYAL SOCIETY OF CHEMISTRY

COMMUNICATION

View Article Online
View Journal | View Issue





Cite this: *J. Mater. Chem. A*, 2025, **13**, 17294

Received 27th February 2025
Accepted 14th May 2025

DOI: 10.1039/d5ta01648g

rsc.li/materials-a

# Precisely engineered conjugated polyimide cathodes with dense redox-active carbonyl sites for superior lithium-ion battery performance†

Mohamed A. Elnaggar,[ab] Nanxi Dong,[ac] Yongjun Kang,[a] Bingxue Liu,[d] Daolei Lin,[a] Guofeng Tian,[a] Shengli Qi *[a] and Dezhen Wu[a]

Polyimide cathode materials have enticed tremendous attention as alternatives to transition-metal electrodes owing to their large theoretical capacity, structural diversity, low cost, and rapid reaction kinetics. Conversely, such imide electrodes still face a severe challenge to achieve their energy storage applications satisfactorily due to the insufficient utilization of their redox-active sites originating from their low electronic conductivities. Herein, four functionalized polyimide composites have been fabricated by virtue of an *in situ* polycondensation reaction between a newly synthesized benzophenone–benzoquinone-based diamine and commercial dianhydrides in the presence of a conductive Super C45 material for application as cathode materials in Li-ion batteries. Such innovative integration of carbonyl groups of benzophenone, benzoquinone, and diimide rings with the Super C45 material not only creates a stable porous structure with abundant accessible redox-active sites but also guarantees fast electron/ion diffusion. Consequently, our targeted PMQP-SP cathode delivers high capacities of 143 mA h $g^{-1}$ at 0.2C and 122 mA h $g^{-1}$ at 1C and attains better rate capability besides ultra-stable cycling performance with 85% capacity retention over 500 cycles at 2C. According to DFT calculations, the theoretical results are well consistent with the electrochemical performance of the synthesized composites. Generally, this work suggests an efficient strategy to design novel carbonyl-rich organic electrodes for next-generation green rechargeable batteries.

## Introduction

Concerning the energy crisis that the world is witnessing nowadays, the development of renewable sustainable energy resources and energy storage technologies has attracted much attention from many researchers to keep pace with the growing demand for energy needs.[1] Lithium-ion batteries (LIBs), which are regarded as the dominant energy storage source in electric vehicles and portable electronics markets, suffer from some problems such as performance constraints, resource shortages, and environmental pollution. On the other hand, the modification and improvement of traditional inorganic electrode materials are no longer sufficient to meet the rapid utilization of clean energy resources due to their intrinsic limitations. Recently, the innovation of redox-organic electrode materials as clean alternatives offering high electrochemical performance with high theoretical capacities, low cost, resource availability, high sustainability, structural diversity, and environmental friendliness was urgently required for next-generation LIBs.[2–7] It is investigated that the optimization of functional groups of redox-organic compounds has a remarkable influence on sufficient conductivity and reversible ion-insertion reactions.[8] Regrettably, the unsatisfactory cycle performance and poor rate capability of rechargeable LIBs were generally achieved due to the critical dissolution of small organic molecules in common electrolytes that minimized their thermal stability.[9,10] So, it was reported that the most effective strategy is to polymerize these small active compounds that could restrain their undesirable solubilities in electrolytes and stabilize redox reactions.[11]

To date, numerous kinds of organic redox-active polymers, including radical polymers,[12–14] organosulfur polymers,[15,16] conductive polymers,[17–20] covalent organic frameworks[21–23] and conjugated carbonyl polymers[24–26] have been examined as polymer-based electrode materials and have attained great success in rechargeable batteries.[27] In particular, it was explored that carbonyl polymers, especially aromatic polyimides, are one of the most promising electrode materials for rechargeable batteries owing to their structural diversity, great thermal

[a]*State Key Laboratory of Chemical Resource Engineering, Beijing University of Chemical Technology, Beijing 100029, China. E-mail: qisl@mail.buct.edu.cn*
[b]*Department of Chemistry, Faculty of Science, Benha University, Benha 13518, Egypt*
[c]*ENFI R&D Institute, China ENFI Engineering Corporation, No. 12 Fuxing Avenue, Haidian District, Beijing 100038, China*
[d]*China Automotive Battery Research Institute Co. Ltd, No. 11 Xingke Dong Street, Yanqi Economic Development Zone Huairou District, Beijing 101407, China*

† Electronic supplementary information (ESI) available. See DOI: https://doi.org/10.1039/d5ta01648g

stability, excellent mechanical strength, high theoretical capacities, and superior electrochemical performance.[28–31] The integration of commercial dianhydrides such as pyromellitic (PMDA), naphthalene-tetracarboxylic (NTCDA), and perylene-tetracarboxylic (PTCDA) with various diamines resulted in electroactive polyimides, which have been successfully applied in rechargeable storage systems.[32–34] It was noticed that each repeating unit of aromatic polyimides predominantly provided two one-electron reduction steps, which mainly depended on the electrochemically active carbonyl groups of dianhydrides.[32] Furthermore, various studies showed that specific capacities and voltage profiles of polyimides can be optimized by changing both dianhydrides and diamines.[32,35] Therefore, polyquinones, as outstanding multi-carbonyl compounds, have achieved high electrochemical performance in rechargeable LIBs.[26,36] Consequently, the insertion of quinone-based moieties into structural polyimide chains was extremely beneficial for their reactivity and has also enhanced their energy densities and specific capacities through lithium enolization of active carbonyl groups.[37] For instance, Wu *et al.* manufactured a novel anthraquinone-based polyimide/SWCNTs composite as a cathode material that exhibited a discharge capacity of 190 mA h $g^{-1}$ at 0.1C.[38] As well, Zhang *et al.* fabricated a core–shell quinone-containing polyimide/CNTs composite, which was employed as a cathode material that delivered a good reversible capacity of 163 mA h $g^{-1}$ at 0.05 A $g^{-1}$.[39] On the other hand, Chen *et al.* designed a novel urea-derived polyimide that was applied as a cathodic material, which offered a specific capacity of 174.5 mA h $g^{-1}$ at 20 mA $g^{-1}$ and a rate capability of 133.5 mA h $g^{-1}$ at 500 mA $g^{-1}$.[40] In contrast, these reported polyimide cathodic materials are still far from practical application owing to their low cycle stability at high current density. Among quinone derivatives, it was investigated that *p*-benzoquinone presented a large theoretical capacity of 496 mA h $g^{-1}$ and a reasonable redox potential of approximately 2–3 V *versus* Li because of its possession of two electroactive carbonyl groups.[41–43] Therefore, it is favorable to insert a benzoquinone moiety into the structural chains of polyimide derivatives that are integrated with abundant Super C45 as a conducting material, which provides an effective, cheap strategy to enhance the electrochemical performance of next-generation rechargeable batteries.

Herein, for the first time, a novel diamine monomer (QDP), including amino benzophenone-terminated benzoquinone, was successfully synthesized through a Michael addition reaction of 1,4-benzoquinone and 4,4′-diamino benzophenone as starting materials under an oxygen atmosphere. To complete our methodology, a new family of multi-carbonyl polyimide composites was fabricated *via* an *in situ* polycondensation reaction between the as-prepared QDP diamine and four different kinds of dianhydrides, such as pyromellitic dianhydride (PMDA), 3,3′,4,4′-biphenyltetracarboxylic dianhydride (BPDA), 4,4′-oxydiphthalic anhydride (ODPA), and benzophenone-3,3′,4,4′-tetracarboxylic dianhydride (BTDA) in the presence of Super C45 as a conducting material. Based on the π–π stacking interaction, the as-fabricated polyimides can be readily incorporated with Super C45 particles for application in Li-ion batteries as organic composite cathodes. Comparatively, the resultant PMQP-SP composite shows distinct chemical/thermal stability with a unique, highly porous structure that significantly shortens pathways for $Li^+$ diffusion. As a consequence, the continuously conjugated PMQP-SP cathode manifests the highest specific capacity of 143 mA h $g^{-1}$ at 0.2C due to larger utilization of its abundant carbonyl groups. Remarkably, a negligible capacity decay is noticed at 2C over 500 cycles with 85% capacity retention, which implies superior long-term cycling stability of the PMQP-SP electrode. Additionally, a large capacity of 122 mA h $g^{-1}$ can be achieved at 1C, demonstrating fast redox reaction kinetics of PMQP-SP, which is possibly further ascribed to its smallest energy gap ($E_g$) relative to other synthesized composites. According to our knowledge, the better rate capability and excellent cycling stability of our PMQP-SP render it among high-performance PI cathodes used for rechargeable batteries.

## Results and discussion

Through the Michael addition reaction, a new (QDP) diamine, containing amino benzophenone-terminated benzoquinone, was successfully synthesized from 1,4-benzoquinone and 4,4′-diamino benzophenone as raw materials for the first time under an oxygen environment (Fig. 1a). In addition, the molar ratio of the reaction can be optimized between 1,4-benzoquinone and 4,4′-diamino benzophenone to be 1 : 2 to obtain a precipitate, which appears with a brown color owing to its benzoquinone structure (Fig. S1†). On the other hand, the chemical structure of QDP diamine was proved *via* $^1$H and $^{13}$C NMR spectral analyses. The $^1$H NMR spectrum exhibits characteristic chemical shifts at 9.52 ppm related to the formed (–NH–) group and 6.16 ppm, which represents the $–NH_2$ group (Fig. S2†). As well, its $^{13}$C NMR spectra display typical chemical shifts at 124.26 ppm, describing the $C–NH_2$ group, and 146.56 ppm, which illustrates the formation of the –C–NH– group, confirming the successful synthesis of the intended QDP structure (Fig. S3†). On the other hand, there is no characteristic peak for oligomers in these spectra, meaning that our product had been completely purified with boiled methanol.

As elucidated in Fig. 1, novel benzoquinone-based polyimide composites (PMQP-SP, BPQP-SP, ODQP-SP, and BTQP-SP) were successfully synthesized through an *in situ* condensation polymerization of the as-synthesized QDP diamine with pyromellitic dianhydride (PMDA) or 3,3′,4,4′-biphenylteteracarboxylic dianhydride (BPDA) or 4,4′-oxydiphthalic anhydride (ODPA) or benzophenone-3,3′,4,4′-tetracarboxylic dianhydride (BTDA), respectively, as commercial dianhydrides in the presence of Super C45 as a conducting material at 180 °C. To affirm that our polyimide composites had been completely imidized, they underwent a thermal treatment at elevated temperatures up to 350 °C under a nitrogen atmosphere. These as-synthesized products have been designed with a special polymeric structure, showing their high insolubility in organic electrolytes, leading to suppressing the undesirable dissolution in these electrolytes during the battery cycling. By highlighting the synthesis mechanism of poly(amic acid), this reaction occurs

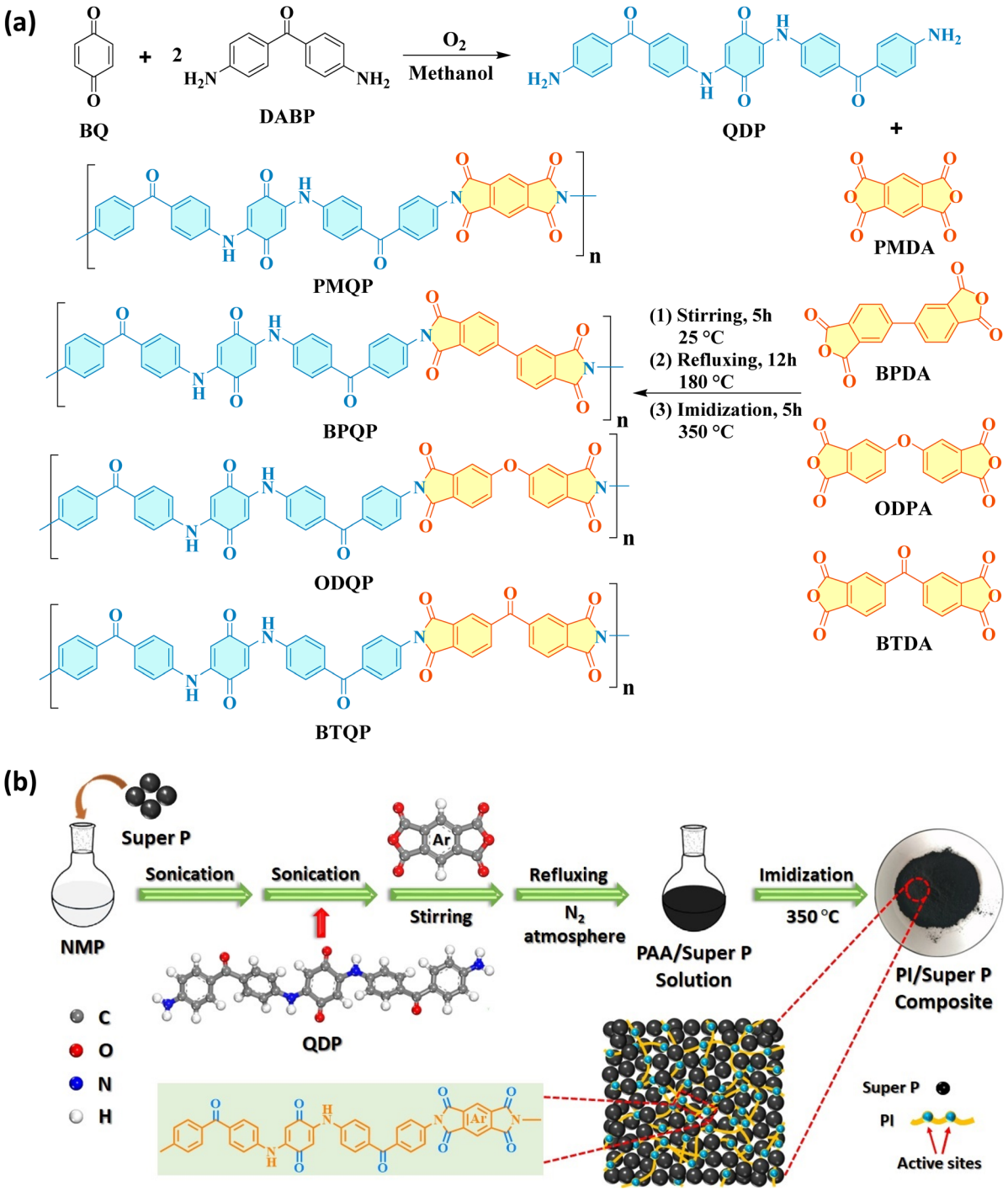


Fig. 1 Synthetic procedures of (a) PMQP, BPQP, ODQP and BTQP polyimides. (b) Polyimide/Super P composites.

*via* the nucleophilic attack of the amino group of the as-prepared QDP diamine on the carbonyl group of the dianhydride monomer, followed by the liberation of water molecules as by-products from PAA to produce polyimide derivatives (Fig. S4 and S5†).

According to the FTIR spectrum shown in Fig. S6,† QDP exhibits peaks at 3463, 3408, and 3342 $cm^{-1}$, attributed to the –$NH_2$ group. In addition, there is a distinct peak at 3268 $cm^{-1}$, which is assigned to the (–NH–) group of the QDP monomer and is still present in the FTIR spectra of our synthesized polyimide materials, emphasizing the successful polymerization process.[8] It is also noticeable that a strong broad peak originated from overlapping two characteristic peaks located at 1855 and 1780 $cm^{-1}$, ascribed to the C=O group of PMDA, besides the appearance of a distinct peak at 1217 $cm^{-1}$, which is assigned to the aryl C–O–C group of PMDA. As for Super P, it displays a small peak at 1583 $cm^{-1}$, attributed to graphitic C=C skeletal vibrations. As illustrated in Fig. 2a, the successful fabrication of

 

the four polyimide composites (PMQP-SP, BPQP-SP, ODQP-SP, and BTQP-SP) was confirmed *via* the appearance of similar characteristic peaks at 1777 and 1725 $cm^{-1}$, corresponding to the stretching vibrations of imide (C=O) groups.[39,40] Additionally, the emerging strong peaks at 1363 $cm^{-1}$ ascribed to the C–N–C group further affirmed the complete imidization process of these polyimide composites, suggesting the formation of imide rings.[38] On the other hand, this FTIR spectrum displays a characteristic peak at 1646 $cm^{-1}$ for these polyimide derivatives that is attributed to the C=O group of the benzoquinone ring, assuring the successful copolymerization process.[8,44] From the elemental analysis data, the practical elements ratios of PMQP-SP, BPQP-SP, ODQP-SP, and BTQP-SP are C%, 81.9; H%, 2.25; N%, 5.49; O%, 10.42, C%, 86.18; H%, 1.98; N%, 3.78; O%, 8.14, C%, 85.57; H%, 1.94; N%, 4.01; O%, 8.52, and C%, 84.7; H%, 2.14; N%, 4.08; O%, 9.12, respectively, which are nearly consistent with their theoretical values, affirming their successful synthesis. As for the Raman spectrum (Fig. S7†), the PMQP polyimide exhibits distinct peaks at 1388.11 and 1240.45 $cm^{-1}$, corresponding to the stretching vibrations of C–N and C–N–C groups, respectively, proving the successful imidization process. In addition, a small peak can be noticed at around 1720.81 $cm^{-1}$, which is assigned to the imide (C=O) groups of PMQP. On the other hand, there is an obvious overlap between the peak of the D band, which is associated with disordered carbon structures of the Super C45 material and the C–N peak of polyimide derivatives at about 1350.99 $cm^{-1}$, affirming the successful synthesis of our polyimide composites. It is also noticeable that a small peak appeared at 845.76 $cm^{-1}$, attributed to the imide ring deformation, further confirming the complete imidization of our polyimide materials.

From the PXRD patterns clarified in Fig. S8,† the PDMA and QDP monomers exhibit sharp distinct peaks at 14.51°, 16.47°, 20.37°, 22°, 28.8°, 30.43° and 8.07°, 11.73°, 12.08°, 12.72°, 14.79°, 16.16°, 17.61°, 23.62°, 24.45°, 29.03°, 32.72°, respectively, denoting their crystalline nature. As for Super P, two significant broad peaks can be observed at 25.07° and 43.44°, corresponding to the (002) and (100) planes of graphite, respectively. Such broad peaks indicate the presence of some graphitic carbon structures within Super P and reflect its amorphous nature. To further examine the internal construction of the synthesized polyimide composites, their XRD patterns were also collected as clarified in Fig. 2b. So, the four composites display analogous two characteristic peaks centered at approximately 25.35° and 43.97° for PMQP-SP, 24.89° and 43.74° for BPQP-SP, 24.25° and 43.78° for ODQP-SP, and 24.97° and 43.85° for BTQP-SP, corresponding to *d*-spacings of 3.51 and 2.06 Å, 3.57 and 2.07 Å, 3.67 and 2.07 Å, and 3.56 and 2.06 Å, respectively. Furthermore, the interplanar spacing of PMQP-SP related to the highest diffraction peak at $2\theta = 25.35°$ is smaller than those of BPQP-SP, ODQP-SP, and BTQP-SP, creating a lower interfacial spacing and boosted intermolecular interactions of the PMQP-SP composite compared to the BPQP-SP, ODQP-SP, and BTQP-SP composites.[45,46] On the other hand,

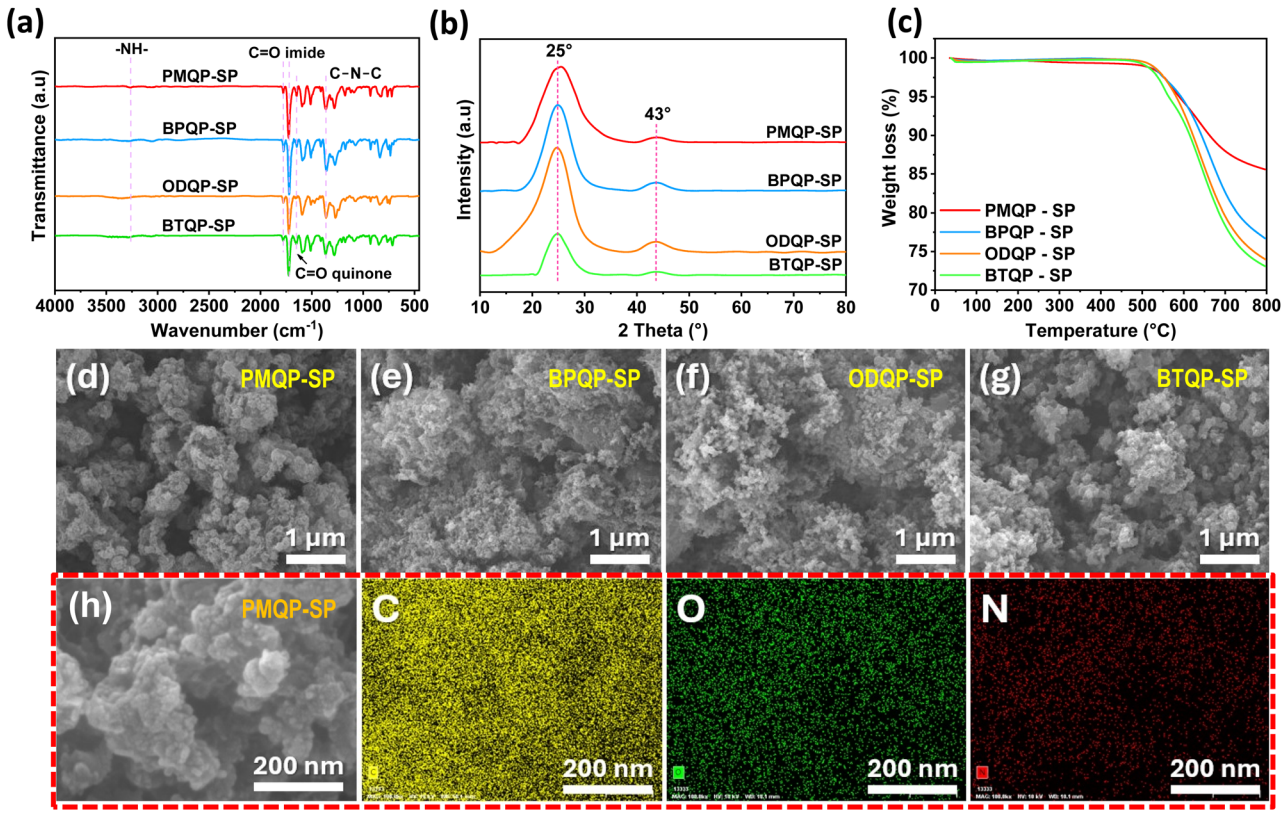


Fig. 2 (a) FTIR spectra. (b) XRD patterns. (c) TGA curves. (d–g) SEM images of PMQP-SP, BPQP-SP, ODQP-SP and BTQP-SP polyimide composites. (h) EDS elemental mapping of the PMQP-SP composite.

the strongest peaks centered at approximately 25° of these polyimide composites that are contributed by the (002) plane of Super C45 indicate the successful mixing of Super C45 particles with polyimide molecules during the nucleation/growth process of these composites.[39] The influence of the molecular structure of these as-synthesized polyimide composites on their thermal stabilities can be explored through thermogravimetric analysis (TGA). As illustrated in Fig. 2c, these polyimide composites exhibit high decomposition temperatures ranging from approximately 530 °C to 547 °C, attributed to their robust structures by virtue of their conjugated aromatic rings. Furthermore, these four composites have high thermal stability and consequently are expected to be applied in lithium-ion batteries with excellent safety during their cycling.

The surface morphologies of the synthesized composites were clearly explored using a scanning electron microscope (SEM). By comparison, PMQP-SP featured a 3D granular-shaped highly porous structure composed of uniformly distributed nanoparticles with an average particle diameter of approximately 888 nm (Fig. 2d), which enlarges the contact interface between the electrolyte and the electrode and suppresses the considerable structural alterations of polyimide chains during battery cycling.[8] On the other hand, the densely agglomerated brick-like morphology can be obviously visualized in BPQP-SP and ODQP-SP (Fig. 2e and f), which largely obstructs the electrolyte infiltration inside these composites. Exceptionally, BTQP-SP displays a colony-like morphology with randomly distributed macropores as shown in Fig. 2g. In conclusion, the unique morphology of PMQP-SP is expected to be favorable for shortening ionic diffusion pathways to the active centers and significantly facilitating the electrolyte permeation inside the cathode during the cycling process, suggesting superior electrochemical performance of PMQP-SP relative to the other composites.[8,39] According to TEM images demonstrated in Fig. S9,† the lattice fringe of our polyimide composites was revealed (inside yellow oval circles). Unfortunately, the lattice fringes of these products aren't obvious enough to calculate their interplanar spacing ($d$). Therefore, our polyimide derivatives are regarded as semicrystalline materials. To further affirm that the homogeneous mixing of polyimide chains with Super C45 molecules happened successfully during the *in situ* polymerization process, the energy dispersive X-ray elemental mapping analysis evidences the uniform spatial distribution of C, O, and N elements inside the as-synthesized composites as illustrated in Fig. 2h and S11–S13.[47] As well, EDS spectra display percentages of C, N, and O elements for each composite (Fig. S10–S13†), which are approximately aligned with their theoretical values, further proving the successful synthesis of these four polyimide composites.

The electrochemical performances of the as-synthesized polyimide composite cathodes were comprehensively investigated through assembling CR2032 coin-type cells using lithium foil as the anode in a potential window of 1.5–3.5 V (*vs.* $Li/Li^+$). To obviously study the lithiation/delithiation behaviors of PMQP-SP, BPQP-SP, ODQP-SP, and BTQP-SP composite cathodes, cyclic voltammetry (CV) of these prepared cathodes was performed at a scan rate of 0.1 mV $s^{-1}$ as illustrated in Fig. 3a–d. By comparison, two distinctive pairs of redox peaks with the highest current density were observed for PMQP-SP (Fig. 3a), denoting the highest electrochemical activity of its carbonyl groups owing to its conjugated structure, suggesting the lowest polarization and largest utilization of its redox carbonyl active sites.[39,48] Additionally, PMQP-SP exhibits two broad reduction peaks; first, at around 2.29 V during the first three cycles and second at approximately 1.92 V in the first cycle, which gradually shifted to a higher potential at 2.01 V in the second cycle and at 2.04 V in the third cycle, as shown in Fig. 3a. This behavior is mainly due to the reduction of active carbonyl groups in both imide and benzoquinone rings, respectively, during the discharging process.[49] On the other hand, two wide oxidation peaks were obviously noticed for PMQP-SP at about 2.39 V during the first three cycles and at around 2.17 V in the first cycle, which slightly moved to lower potential at 2.15 V throughout the second and third cycles, which can be attributed to the oxidation of carbonyl groups of quinone and imide moieties during the charging process.[49] According to Fig. 3b, BPQP-SP also displays two weak reduction peaks at about 2.52 and 1.77 V with three broad oxidation peaks at 1.99, 2.49, and 2.81 V during the first three cycles, which may be due to the enolization reaction of carbonyl groups in imide units.[44] Unfortunately, the redox behavior of carbonyl groups of the imide unit and benzoquinone ring based on ODQP-SP was not observed clearly as clarified in Fig. 3c, referring to its poor electrochemical activity, in good agreement with its lowest discharge capacity. As well, the lowest peak current of ODQP-SP confirms the worst redox activity, which may be ascribed to broken electron transfer channels.[39] Furthermore, two weak reduction peaks located at 2.51/1.76 V and three broad oxidation peaks appeared at 2.14/2.47/2.81 V and were monitored for BTQP-SP during the first three cycles, as elucidated in Fig. 3d, owing to successive lithiation/delithiation processes of carbonyl groups of imide and quinone units as well as the enolization of BTDA-based bridged carbonyl groups. From the whole CV data, these polyimide composites have acceptably stable lithiation and delithiation behaviors except ODQP-SP, due to better electrochemical activity of their carbonyl groups in both imide and benzoquinone moieties, leading to accommodation of multiple lithium ions, which contribute to achieving large specific capacity. As demonstrated in the galvanostatic charge–discharge profiles, two obvious redox plateaus for PMQP-SP and unclear voltage plateaus for BPQP-SP, ODQP-SP, and BTQP-SP cathodes can be observed at 0.2C (Fig. 3e), which are in good agreement with their CV curves, implying higher redox activity of PMQP-SP than those of BPQP-SP, ODQP-SP, and BTQP-SP cathodes. It is also noticeable that the average discharge voltage of PMQP-SP is higher than those of BPQP-SP, ODQP-SP, and BTQP-SP, owing to the highly stable conjugated structure of PMQP-SP, which could lower its (LUMO) energy levels, suggesting larger utilization of active sites.[8,50]

The cycling performances of these as-synthesized composites were evaluated as LIB cathodes by assembling them into CR2032 coin-type cells. As well, their discharge capacities were recorded based on the mass loading of active materials (PMQP, BPQP, ODQP, and BTQP) inside the cathode slurry, which is

 

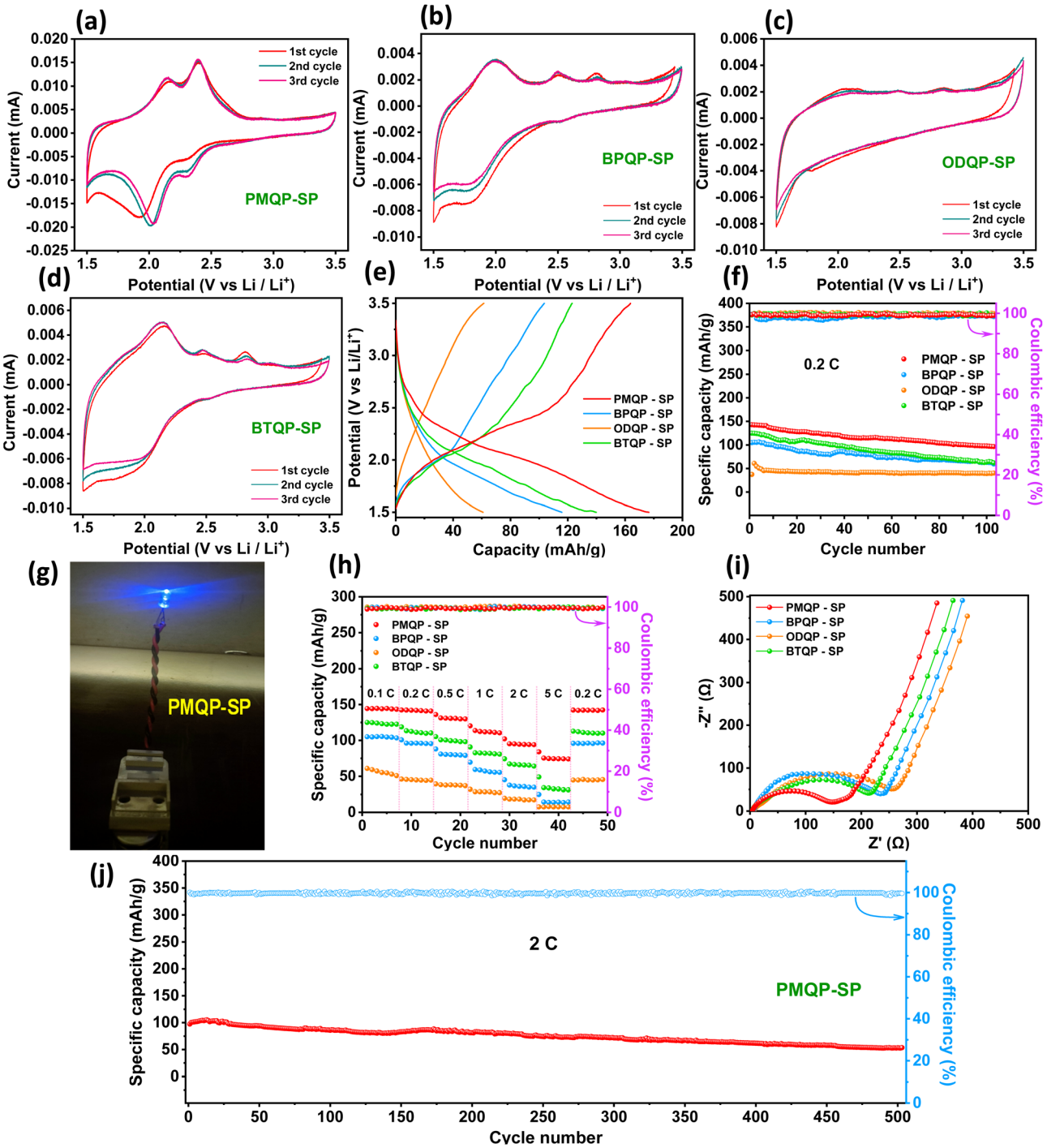


Fig. 3 Electrochemical performances of synthesized polyimide composites as LIB cathodes. (a–d) CV curves of PMQP-SP, BPQP-SP, ODQP-SP and BTQP-SP at a scan rate of 0.1 mV $s^{-1}$. (e) Charge–discharge profiles. (f) Cycling performances of PMQP-SP, BPQP-SP, ODQP-SP and BTQP-SP at 0.2C. (g) Optical image of a PMQP-SP cathode-based $Li^+$ battery for powering an LED bulb. (h) Rate performances at different current densities. (i) EIS of PMQP-SP, BPQP-SP, ODQP-SP and BTQP-SP in the frequency range of 0.01–100 000 Hz. (j) Long-term cycling stability of PMQP-SP at 2C.

around 0.4 mg $cm^{-2}$.[47,51,52] To study the influence of the Super C45 additive as a conducting material inside the fabricated composite during the cycling process, the PMQP-Super C45 composite was prepared with different ratios of Super C45 during the *in situ* polymerization resulting in PMQP-SP (15%), PMQP-SP (25%), and PMQP-SP (35%), for instance. By increasing the amount of the Super C45 material in this composite, its average discharge capacity is largely reinforced from 44 mA h $g^{-1}$ for PMQP-SP (15%) to 83 mA h $g^{-1}$ for PMQP-SP (35%) during 100 cycles at 0.5C as shown in Fig. S14.† This

behavior is mainly attributed to the considerable improvement of the electronic conductivity of this composite originating from Super C45, which can be ascribed to the formation of a conductive hetero-architecture by virtue of an *in situ* polymerization, guaranteeing larger utilization of redox-active carbonyl groups, delivering higher discharge capacity.[52] On the other hand, the specific capacity of Super C45 is considered to be negligible in terms of LIB electrochemical capacity because it is a highly disordered form of carbon, which is treated as electrochemically inactive. Therefore, its discharge capacity was revealed to be around 14 mA h $g^{-1}$ at 0.2C over 100 cycles (Fig. S15a†), mostly because of its surface adsorption or pseudocapacitive effects, not the bulk intercalation during battery cycling. As expected, Super C45 presented ultra-weak redox peaks during the initial three cycles in the CV test (Fig. S15b†), affirming its poor cycling behavior. So, this composite was optimally synthesized with 45% of Super C45 to yield PMQP-SP, which significantly delivers ultra-stable specific capacity reaching 122 mA h $g^{-1}$ over 100 cycles with 90% capacity retention and an excellent Coulombic efficiency of 99.1% at the same current rate (Fig. S16†). In order to obviously investigate the effect of the chemical structure of polyimides on their cycling behavior, these as-synthesized PMQP-SP, BPQP-SP, ODQP-SP, and BTQP-SP composites were tested at a current density of 0.2C (Fig. 3f). Notably, $a \approx 91\%$ capacity retention is attained for PMQP-SP, which retains a superior capacity of 130 mA h $g^{-1}$ after 100 cycles compared with BTQP-SP, BPQP-SP, and ODQP-SP, demonstrating the highly stable chemical structure of PMQP-SP. Additionally, the PMQP-SP electrode exhibits a stable, excellent Coulombic efficiency of up to 99.8% relative to BPQP-SP, ODQP-SP, and BTQP-SP. Exceptionally, the ODQP-SP cathode displays a stable cycling behavior with a limited capacity of around 40 mA h $g^{-1}$, attributed to the low utilization of its active carbonyl sites. Remarkably, BTQP-SP and BPQP-SP largely suffer from capacity fading during 100 cycles, achieving the lowest capacity retention of approximately 49.7% and 56.7%, respectively, which can be ascribed to their poorest structural stability. Moreover, the full battery based on our targeted PMQP-SP cathode can successfully illuminate an LED bulb with stable lighting (Fig. 3g), elucidating its actual application as an organic cathode for rechargeable LIBs.

In order to evaluate the rate capabilities of these PMQP-SP, BPQP-SP, ODQP-SP, and BTQP-SP cathodes, their performance was obviously examined at different current densities, which were increased stepwise from 0.1C to 5C. Remarkably, the PMQP-SP cathode manifests the largest discharge capacities and better rate performance with increasing the current density to 5C compared to those of BTQP-SP, BPQP-SP, and ODQP-SP cathodes (Fig. 3h), which can be attributed to the highly porous morphology and stable conjugated structure of PMQP-SP, leading to fast reaction kinetics. Notably, PMQP-SP delivers the highest discharge capacitances of 144, 142.5, 131, 113, 95, and 75 mA h $g^{-1}$ at current densities of 0.1C, 0.2C, 0.5C, 1C, 2C, and 5C, respectively, achieving an excellent Coulombic efficiency of 99.6%. Additionally, the specific capacity of PMQP-SP is retrieved to 142.3 mA h $g^{-1}$, when the current density decreases to 0.2C again, achieving a capacity retention of approximately 99.86% of its initial value. Exceptionally, the satisfactory rate capability of BTQP-SP to some extent was observed through displaying acceptable discharge capacities of 125 mA h $g^{-1}$ at 0.1C and 34 mA h $g^{-1}$ at 5C, which are higher than those of BPQP-SP and ODQP-SP cathodes as clarified in Fig. 3h. Compared with BPQP-SP and ODQP-SP, the enhanced performance of the BTQP-SP cathode with a high Coulombic efficiency of 99.3% is possibly ascribed to the conjugation of p-orbitals of BTDA-based bridged carbonyl groups with π-orbitals of aromatic rings, subsequently creating electron transport channels leading to boosting the charge delocalization during the cycling process, contributing to the additional discharge capacity.[53] As for BPQP-SP and ODQP-SP cathodes, they exhibit the worst rate capabilities, owing to the decay of their specific capacities from 105 mA h $g^{-1}$ at 0.1C to 14.3 mA h $g^{-1}$ at 5C for BPQP-SP and from 60.9 mA h $g^{-1}$ at 0.1C to 7.6 mA h $g^{-1}$ at 5C for ODQP-SP as shown in Fig. 3h. Their poorest electrochemical activities may be attributed to obstruction of the electron transportation along polyimide chains because of the cleavage of their conjugated BPDA and ODPA units during the battery cycling.[39] On the other hand, the PMQP-SP cathode attains the largest capacity retention of about 52.1% at a high current density of 5C compared to BTQP-SP (retention $\sim$ 27.2%), BPQP-SP (retention $\sim$ 13.6%), and ODQP-SP (retention $\sim$ 12.5%), affirming the highest rate capability of PMQP-SP relative to the other prepared cathodes.

Furthermore, Fig. S17† illustrates the charge–discharge curves of the PMQP-SP cathode at various current densities. As expected, two characteristic discharge/charge plateaus can be obviously noticed, which are aligned with the two pairs of redox peaks in the CV analysis (Fig. 3a), assuring two consecutive lithiation/delithiation processes during the cycling process. It is noticeable that these profiles display a similar trend with a slight expected alteration of polarization within a wide range of the current rate, signifying the high structural stability of the PMQP-SP composite, leading to fast reaction kinetics during the battery operation.[54] In order to deeply understand the reaction kinetics of these polyimide composites, their electrochemical performance was further explored *via* electrochemical impedance spectroscopy (EIS). Through Nyquist plots demonstrated in Fig. 3i, PMQP-SP manifests the lowest charge transfer resistance ($R_{ct}$ = 147.6 Ω) compared with BPQP-SP ($R_{ct}$ = 234.4 Ω), ODQP-SP ($R_{ct}$ = 254.3 Ω), and BTQP-SP ($R_{ct}$ = 214.6 Ω), implying faster ionic transport and higher electronic conductivity for PMQP-SP.[8] This behavior can be attributed to the integration of the continuously conjugated system of the pyromellitic dianhydride unit of PMQP with Super C45 particles, resulting in the creation of more electron transfer channels and then significantly lowering the charge transport impedance. The EIS results are consistent with the cycling performances of the as-fabricated polyimide cathodes at a current density of 0.2C (Fig. 3f), which may be attributed to their wettability by the liquid organic electrolyte. By highlighting their wetting behavior, these prepared polyimide composites are thought to have an enhanced contact between polyimide chains and the conductive additive by virtue of *in situ* polymerization, which diminishes their polymeric swelling into the electrolyte based

 

on functionality.[55] Consequently, the PMQP-SP composite has the smallest aryl segment, generating the lowest swelling in the liquid electrolyte compared with BPQP-SP, ODQP-SP, and BTQP-SP composites, manifesting the lowest charge impedance for PMQP-SP. On the other hand, the BTQP-SP composite shows lower charge transfer resistance in comparison with BPQP-SP and ODQP-SP, as elucidated in Fig. 3i. This behavior can be ascribed to the additional bridged-carbonyl group of BTQP-SP, which may create more electronic cloud, suggesting faster charge transfer in BTQP-SP relative to BPQP-SP and ODQP-SP.

To further explore the long-term cycling performance of the targeted PMQP-SP composite, the galvanostatic charge–discharge test was carried out at 1C and 2C over 300 and 500 cycles, respectively (Fig. S18† and 3j). At current densities of 1C and 2C, high capacities of up to 108 mA h $g^{-1}$ and 83 mA h $g^{-1}$ could still be retained with a high capacity retention of 89% and 85% for the PMQP-SP cathode even after 300 and 500 cycles, respectively, signifying its ultra-stable long-term cycling behavior and high structural stability. In addition, this composite achieves superior Coulombic efficiencies, reaching approximately 99.6% and 99.5% at 1C and 2C, respectively, reflecting its ultra-stable reversible redox behavior. Such cycling stability of PMQP-SP can be ascribed to its highly porous structure with abundant accessible active carbonyl sites as well as the strong interaction between PMQP and Super C45, boosting its electronic conductivity. Furthermore, the chemical structure of PMQP polyimide was stabilized by virtue of the aniline segment, which significantly minimized the steric hindrance originated from the proximity of imide and benzoquinone moieties to each other, further facilitating the accommodation of lithium ions at active carbonyl groups.[8] Last but not least, our PMQP-SP cathode displayed superior cycling performance relative to the reported polyimide electrode materials for rechargeable batteries (Table S1†).

In order to deeply investigate the intrinsic dynamics and the electrochemical reaction kinetics associated with lithium ion storage in the PMQP-SP cathode, CV measurements were performed at different scan rates ranging from 0.1 mV $s^{-1}$ to 1 mV $s^{-1}$. As demonstrated in Fig. 4a, by increasing the scan rate in the CV test, all curves are obviously identical, signifying the ultra-stable electrochemical behavior and excellent reversibility of the PMQP-SP cathode.[54] Exceptionally at higher scan rates, an additional reduction peak (R3) is obviously noticed at 1.75 V, which is not present in the previous CV test (Fig. 3a), attributing to larger utilization of highly active carbonyl groups to form lithium enolate and thus contributing to higher specific capacity for PMQP-SP. Additionally, redox peak currents increase gradually with increasing the scan rate with slight shifts, which are the result of the polarization effect.[54] On the other hand, the redox reaction obeys semi-infinite linear diffusion according to the following eqn (1):[52,56]

$$i = av^b \quad (1)$$

giving a $b$ value of 0.5, while this value is 1 for the capacitive process. As shown in Fig. 4b, the $b$ values of five redox peaks were calculated to be 0.89, 0.88, 1, 0.92, and 0.84, which are close to 1. These values illustrate that the lithium storage in PMQP-SP is a rapid surface-controlled pseudocapacitive process, which is originated from the high reactivity of imide and benzoquinone rings in PMQP-SP and infinite ionic diffusion inside the aligned channels.[52]

In order to deeply explore the redox behavior of our polyimide cathode materials during the lithiation–delithiation process, the *ex situ* FTIR analysis was conducted for PMQP-SP. As clarified in Fig. 4c, the peaks at 1723 and 1645 $cm^{-1}$ can be observed, attributed to the C=O stretching vibrations of imide and benzoquinone rings, respectively. During the discharge process, the C=O peaks gradually diminish based on the insertion of lithium ions, which bind with redox-active carbonyl groups to form lithium enolate groups (C–O–Li), affirming the appearance of a new peak at 1435 $cm^{-1}$ that gradually becomes stronger when the cathode is completely discharged. It is also noticeable that the emerging C–O–Li peak gradually fades away besides the increase of the C=O peaks' intensity progressively when the electrode returns to the charge state, referring to the stable reversible redox reactions of active carbonyl groups during the cycling process. On the other hand, the lithium storage mechanism of the PMQP-SP composite cathode can theoretically be proposed as shown in Fig. 4d. It is believed that PMQP-SP significantly inclines to accommodate/release six lithium ions at the negatively charged carbonyl groups for each repeating unit during the discharging/charging process, achieving a theoretical specific capacity of 226 mA h $g^{-1}$.[39,52] However, the practical capacities of PMQP-SP obtained during galvanostatic charge/discharge measurements are lower than the theoretical value, which may be ascribed to alteration of molecular conformations of PMQP polyimide, creating a slight steric hindrance along polyimide chains during the lithiation process.[39]

After cycling at 0.2C for 100 cycles, the surface morphologies of PMQP-SP, BPQP-SP, ODQP-SP, and BTQP-SP electrodes are obviously studied through SEM images (Fig. 5a–h). Generally, the pristine PMQP-SP, BPQP-SP, ODQP-SP, and BTQP-SP cathodes display similar morphologies with uniformly distributed and integrated structures without any defects (Fig. 5a, c, e and g), which can be attributed to the *in situ* polymerization of these composites.[55] It is noticeable that the cycled PMQP-SP electrode retained a smooth contact surface with negligible changes even after 100 cycles (Fig. 5b), reflecting its high structural stability, which was further preserved by the Super C45 additive. In contrast, the surfaces of cycled BPQP-SP, ODQP-SP, and BTQP-SP cathodes became brittle and relatively rough with numerous large random porous cracks (Fig. 5d, f and h). This cracking may be ascribed to the unconfined swelling of BPQP, ODQP, and BTQP polyimide fragments during the cycling process because of their larger structure sizes relative to PMQP as well as their intense dissolution into the liquid electrolyte during the battery operation.[55] The surface morphologies of our cycled polyimide composite cathodes are well consistent with their electrochemical performances.

Interestingly, polyimide electrode materials are generally insoluble in organic electrolytes, ensuring better electrochemical performance upon long-term cycling. Therefore, the

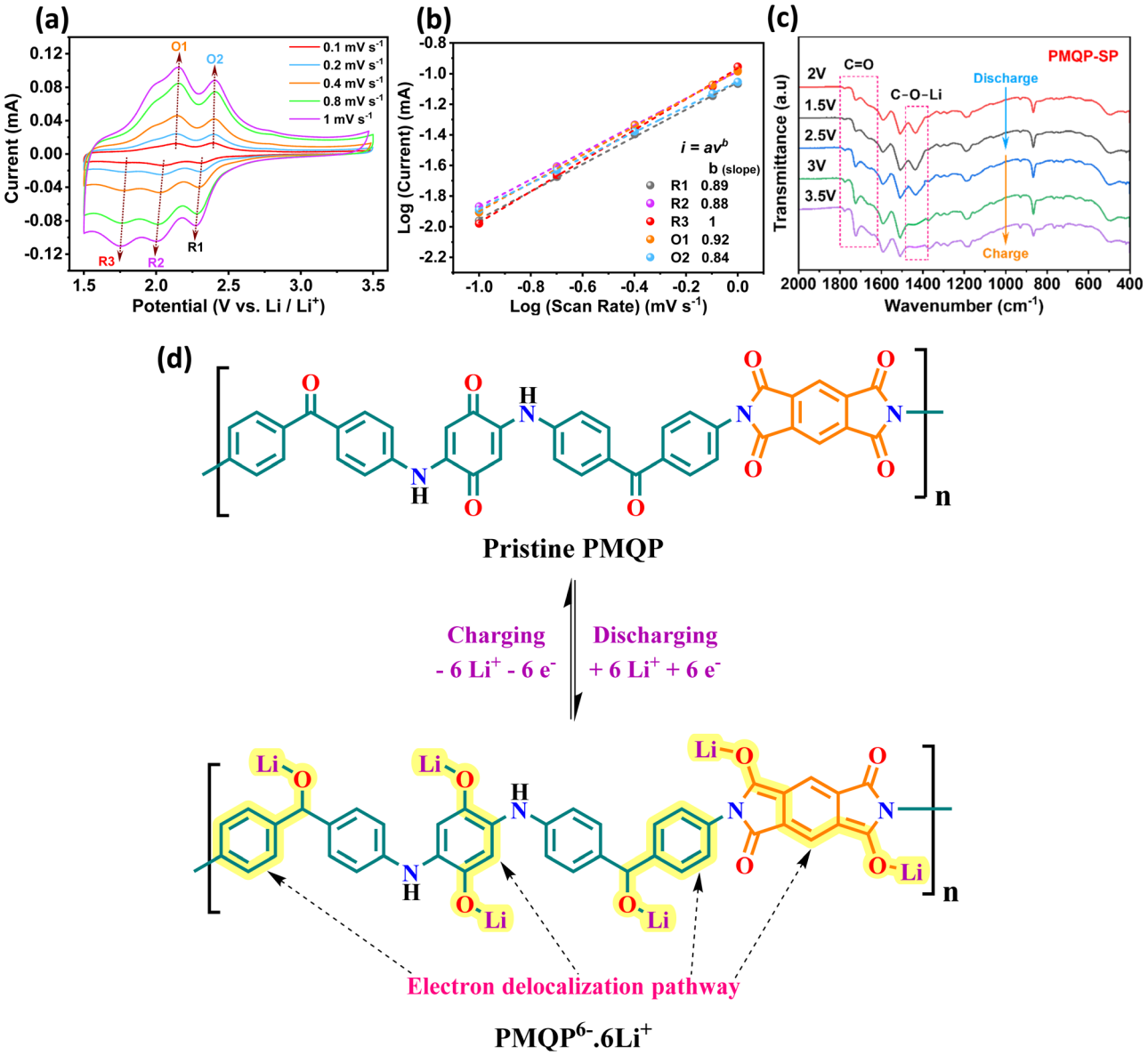


Fig. 4 Kinetics analysis of the PMQP-SP cathode. (a) CV curves at different scan rates. (b) The linear plots of log(*i*) *versus* log(*v*). (c) *Ex situ* FTIR spectra of the PMQP-SP cathode at different states during the first cycle. (d) The proposed Li-ion storage mechanism of the PMQP-SP cathode during the charging–discharging process.

degradation behavior of our polyimide composites was examined *via* their immersion in the 1 M LiTFSI (DOL : DME) electrolyte for 14 days (Fig. S19†). Remarkably, there is no turbidity caused by our polyimide cathode materials after the immersion in this organic electrolyte, reflecting their high resistance to unwanted dissolution in this electrolyte throughout the battery cycling. On the other hand, the surface morphology of these immersed polyimide cathodes was explored through SEM images (Fig. S20†). As expected, our polyimide composites display no visible cracks following immersion, further signifying their stable mechanical integrity and high structural stability. Generally, the electrode–electrolyte interaction plays a key role in the electrochemical behavior of the electrode.[8] By highlighting the PMQP-SP cathode as an example, its cycling performance was explored at 0.5C over 100 cycles in different electrolytes. By comparison, $a \approx 90\%$ capacity retention is achieved for PMQP-SP using the 1 M LiTFSI (DOL : DME) electrolyte, which is more than that using the 1 M $LiPF_6$ (EC : DME : EMC) electrolyte (rapid capacity decay; CR $\approx$ 24%), aligning with Coulombic efficiency results as shown in Fig. S21a.† On the other hand, the PMQP-SP cathode displays better rate capability utilizing the 1 M LiTFSI (DOL : DME) electrolyte than that utilizing the 1 M $LiPF_6$ (EC : DME : EMC) electrolyte (Fig. S21b†). As for the charge–discharge curves in the case of using the 1 M $LiPF_6$ (EC : DME : EMC) electrolyte at different current rates (Fig. S21c†), a larger gap between the charge and discharge plateaus can be observed,[57] which implies larger polarization upon cycling in comparison with the charge–discharge profiles

 

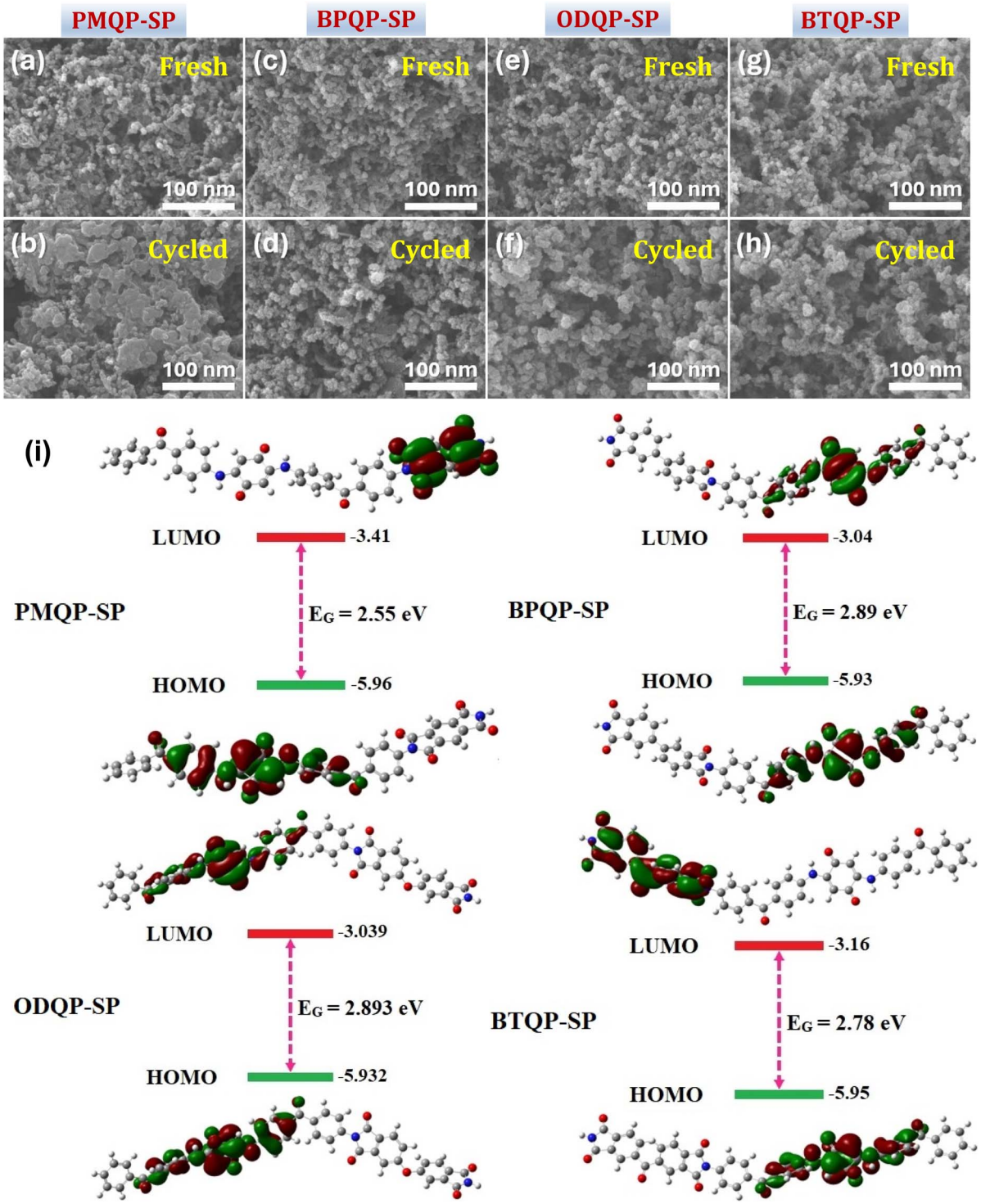


Fig. 5 SEM images of (a), (c), (e) and (g) fresh and (b), (d), (f) and (h) cycled PMQP-SP, BPQP-SP, ODQP-SP and BTQP-SP cathodes at 0.2C for 100 cycles. (i) Energy level diagram of the HOMO/LUMO energy gap for PMQP-SP, BPQP-SP, ODQP-SP and BTQP-SP.

in the case of using the 1 M LiTFSI (DOL : DME) electrolyte (Fig. S17†).

To realize the electrochemical performance of PMQP-SP, BPQP-SP, ODQP-SP, and BTQP-SP polyimide composites in a deeper and clearer sense, the energy levels of the highest occupied molecular orbital (HOMO) and lowest unoccupied molecular orbital (LUMO) of these polyimide derivatives were calculated using density functional theory (DFT) with the help of the B3LYP functional and 6-31+G(d) basis sets using a Gaussian 09 program to analyze their energy gaps ($E_g$) (Fig. 5i). Basically, the lower the LUMO–HOMO energy gap of any compound, the higher the oxidizability and reducibility

processes inside Li-ion batteries, leading to improvement of their electrochemical performances.[32] According to the molecular orbital theory, the energy gap ($E_g$) can detect the electronic conductivity of any electrode material, which may be attributed to its polarization.[40,58] Fortunately, the carbonyl group can lower (LUMO) energy levels of polyimide derivatives, which enhances their ability to be reduced to enol form.[59] Based on the DFT results, there is a large convergence between HOMO energies of the as-synthesized polyimide materials, as clarified in Fig. 5i, owing to the existence of an electron-withdrawing influence originated from benzoquinone and benzophenone segments.[8] Notably, PMQP-SP has the lowest LUMO energy with the smallest energy gap value compared with BPQP-SP, ODQP-SP, and BTQP-SP, resulting in superior redox reversibility and higher electronic conductivity of PMQP-SP, which lead to high cycle stability and better rate capability, probably because of the strongest continuous aromatic conjugation effect of PMQP-SP.[39,53] As demonstrated in Fig. 5i, BTQP-SP with an additional carbonyl bridged group displays a lower $E_g$ value than BPQP-SP and ODQP-SP, which facilitates electron transfer, owing to the p–π conjugation property of BTQP-SP.[39] These DFT results are in good agreement with the electrochemical performance of our polyimide composites. In order to further understand the lithium storage behavior of our as-synthesized composites, their electrostatic potential (ESP) maps were computed using the DFT calculations as clarified in Fig. S22.† According to these maps, the electron-withdrawing carbonyl groups significantly incline to be electrochemically active sites for lithium accommodation more than other segments along polyimide chains, owing to their negative ESP values.[52] On the other hand, the structural evolution of PMQP-SP could be further explored during the lithiation/delithiation process (Fig. S23†), which can be predicted by virtue of the electrostatic potential mapping of PMQP-SP as shown in Fig. S22.† Remarkably, the carbonyl groups located in the yellowish red areas with the most negative ESP values are highly active to bind lithium ions at a relatively high potential, leading to modification of the 3D structure of PMQP-SP to create a stable state during the lithiation process.[53,60]

# Experimental

## Materials

Pyromellitic dianhydride (PMDA, 99%), 3,3′,4,4′-biphenylteteracarboxylic dianhydride (BPDA, ≥99%), 4,4′-oxydiphthalic anhydride (ODPA, ≥99%), benzophenone-3,3′,4,4′-tetracarboxylic dianhydride (BTDA, 99%), and poly(vinylidene fluoride) (PVDF, average $M_w \sim 534\,000$) were purchased from Shanghai Aladdin Biochemical Technology Co., Ltd and utilized as received. Also, 1,4-benzoquinone (BQ, 99.5%) and 4,4′-diamino benzophenone (DABP, 98%) were obtained from Shanghai Macklin Biochemical Co., Ltd and used without further purification. As for solvents, 1-methyl-2-pyrrolidinone (NMP, >99%) was purchased from Shanghai Macklin Biochemical Co., Ltd, while methanol (≥99.9%) was obtained from Shanghai Aladdin Biochemical Technology Co., Ltd and used as received. Super C45 (SP, Timical) was supplied by the China Automotive Battery Research Institute and utilized without further purification.

## Characterization

The chemical structures of synthesized compounds were confirmed *via* a Thermo Scientific Nicolet iS5 FT-IR spectrometer with the aid of KBr pellets in the 400–4000 $cm^{-1}$ regime. The Raman spectrum of synthesized polyimide derivatives was obtained on a Renishaw inVia Reflex using a 514 nm excitation laser with 0.1% laser power in the 100–3200 $cm^{-1}$ range. $^1H$ and $^{13}C$ NMR spectra were collected on a Bruker Avance 600 MHz spectrometer, which was used to perform 16/2048 scans for $^1H/^{13}C$ NMR at 298 K in deuterated DMSO-$d_6$ as a solvent and tetramethyl silane (TMS) as an internal reference to affirm the chemical structure of the synthesized QDP diamine. The element ratios of our samples were measured on a Vario EL cube elemental analyzer (Elementar Analysensysteme GmbH) at a decomposition temperature of 950–1200 °C. The thermal stabilities of polyimide composites were tested using a thermogravimetric analyzer (TGA, Q50) under a nitrogen atmosphere with a heating rate of 10 °C $min^{-1}$ from ambient temperature to 800 °C. Powder X-ray diffraction (XRD) patterns of fabricated composites were obtained using a Rigaku SmartLab SE diffractometer in the 3–90° range with a scanning rate of 5° $min^{-1}$. The surface morphologies of polyimide composites and their cathodes were explored using a JSM-7800F Schottky field emission scanning electron microscope (SEM, JEOL). The internal surface morphology of our polyimide products was revealed using a HITACHI high-resolution transmission electron microscope (TEM, HT7700). The elemental mapping of synthesized composites was investigated using a Bruker Energy Dispersive X-ray spectrometer (EDS, XFlash 6160).

## Synthetic procedures

**Synthesis of QDP diamine.** First, a quantity of 4,4′-diamino benzophenone (DABP, 1.294 g, 6.1 mmol) was dissolved well into 120 ml of pure hot methanol in a 250 ml round-bottom flask *via* magnetic stirring. Based on the complete solubility of DABP, a small amount of 1,4-benzoquinone (0.324 g, 3 mmol) dissolved in 6.5 ml of pure methanol was added dropwise to the DABP solution with a mild stirring in a closed system under an oxygen atmosphere as an oxidant at ambient temperature. During the reaction, the solution color gradually changed from yellow to red and finally appeared as a deep brown color with small quantities of sediments. Under monitoring of the reaction, the precipitate amount gradually increased with increasing time. After the completion of the reaction, the brown sediments were filtered, washed various times with boiled methanol to remove any byproducts and unreacted monomers, and finally dried overnight in a vacuum oven at 65 °C. On the other hand, the product yield was 27%. According to the elemental analysis results, the practical elements percentages of QDP are C%, 72.32; H%, 4.63; N%, 10.53; O%, 12.58, which are completely aligned with their theoretical percentages (C%, 72.71; H%, 4.59; N%, 10.6; O%, 12.11), confirming its high purity. $^1H$ NMR (600 MHz, DMSO-$d_6$, $\delta$): 6.09 (s, 2H), 6.16 (s,

 

4H), 6.62 (d, 4H), 7.55 (dd, 8H), 7.68 (d, 4H), and 9.52 (s, 2H) (Fig. S2†). $^{13}$C NMR (600 MHz, DMSO-$d_6$, $\delta$): 97.49, 113.04, 122.96, 124.26, 130.70, 133.02, 135.76, 141.05, 146.56, 154.21, 180.79, and 192.74 (Fig. S3†).

**Synthesis of PMQP-SP, BPQP-SP, ODQP-SP and BTQP-SP polyimide composites.** According to our optimization, a 25 ml three-necked flask was charged with a controlled amount of Super C45 (45% of the product yield), which was ultrasonically dispersed into 10 ml of 1-methyl-2-pyrrolidinone (NMP) for 45 min. Thereafter, 211 mg (0.4 mmol) of QDP and 88 mg (0.4 mmol) of PMDA were added into this dispersed solution to be dissolved well through further sonication for 15 min. Under an $N_2$ atmosphere, this mixture was stirred vigorously for 5 h at room temperature to form poly(amic acid) followed by refluxing at 180 °C for 12 h. After the reaction completion, the resulting mixture was cooled to ambient temperature and poured dropwise into 100 ml of methanol with stirring to obtain polyimide composite sediments. As well, the as-synthesized product was washed with hot methanol and acetone numerous times, collected by filtration under vacuum, and then dried in a vacuum oven at 120 °C for 12 h. Finally, this composite was completely imidized through thermal treatment at 350 °C for 5 h under a nitrogen atmosphere. For the synthesis of other polyimide composites by the same procedures, the PMDA monomer was replaced with BPDA (119 mg, 0.4 mmol) or ODPA (125 mg, 0.4 mmol) or BTDA (130 mg, 0.4 mmol) dianhydrides. The polyimide composites fabricated from PMDA, BPDA, ODPA, and BTDA dianhydrides were named PMQP-SP, BPQP-SP, ODQP-SP, and BTQP-SP, respectively.

### Fabrication of organic cathodes

Active materials (synthesized polyimide composites) were mixed with a conductive carbon filler (Timical Super C45) and binder (polyvinylidene fluoride) with a weight ratio of 6 : 3 : 1 and vigorously stirred in 1-methyl-2-pyrrolidinone (NMP) for 7 h to form a homogeneous slurry. Then, this slurry was pasted onto aluminum foil, which worked as the current collector, and dried under vacuum for 10 h at 80 °C, followed by cutting the dried foil into coin species to produce polyimide cathodes.

### Battery assembly

To assemble a full battery successfully, the as-prepared cathodes were gathered with metallic lithium as the anode in the presence of a microporous membrane (Celgard-2400) as the separator in an argon-filled glove box to create CR2032 coin-type cells for electrochemical measurements. As well, these three parts were immersed into the electrolytic solution, which was 1 M LiTFSI dissolved in a mixture of 1,3-dioxolane (DOL) and 1,2-dimethoxyethane (DME) (1 : 1 volume%).

### Electrochemical measurements

The battery performance was examined using a LAND CT2001A battery cycler at different current densities within a potential window of 1.5–3.5 V at room temperature. On the other hand, the cyclic voltammetry (CV) tests were carried out on a CHI660C electrochemical workstation at various scan rates ranging from 0.1 mV $s^{-1}$ to 1 mV $s^{-1}$ in the voltage range of 1.5–3.5 V. As well, the electrochemical impedance spectroscopy (EIS) measurements were conducted on the same electrochemical workstation at an oscillation amplitude of 5 mV in the frequency range from 100 kHz to 0.01 Hz at room temperature.

## Conclusions

In summary, a novel series of multi-carbonyl polyimide composites bearing different dianhydride linkers were successfully manufactured *via* an *in situ* polymerization technique in the presence of a Super C45 additive and employed as organic cathodes in rechargeable LIBs. Comparatively, the PMDA-based polyimide composite (PMQP-SP) offers the largest specific capacities of 143 mA h $g^{-1}$ at 0.2C and 122 mA h $g^{-1}$ at 1C and highly stable long-term cycling behavior with 85% capacity retention at 2C, achieving excellent Coulombic efficiency up to nearly 100%, mainly owing to its highly porous stable structure and larger utilization of its abundant redox-active carbonyl sites. Additionally, the charge storage in the PMQP-SP cathode is detected as a rapid pseudocapacitive process. Based on DFT calculations, the energy gap results of our polyimide composites are in good agreement with their electrochemical performances. Our strategy provides a new vision to develop superior-performance organic electrodes for application in next-generation green rechargeable batteries.

## Data availability

The data supporting this article have been included as part of the ESI.†

## Author contributions

M. A. E.: conceptualization, data curation, formal analysis, investigation, methodology, software, visualization, writing – original draft, and writing – review & editing. N. D.: investigation and methodology. Y. K.: methodology, software, and visualization. B. L.: methodology and writing – review & editing. D. L.: writing – review & editing. G. T.: formal analysis. S. Q.: funding acquisition, project administration, resources, supervision, validation, visualization, and writing – review & editing. D. W.: supervision and validation.

## Conflicts of interest

There are no conflicts to declare.

## Acknowledgements

This work was financially supported by the National Natural Science Foundation of China (51673017 and 21404005) and the Fundamental Research Funds for the Central Universities (XK1802-2).

## Notes and references

1 M. Armand and J.-M. Tarascon, *Nature*, 2008, **451**, 652–657.
2 S. Li, K. Wang, G. Zhang, S. Li, Y. Xu, X. Zhang, X. Zhang, S. Zheng, X. Sun and Y. Ma, *Adv. Funct. Mater.*, 2022, **32**, 2200796.
3 B. Zhu, L. Fan, N. Mushtaq, R. Raza, M. Sajid, Y. Wu, W. Lin, J.-S. Kim, P. D. Lund and S. Yun, *Electrochem. Energy Rev.*, 2021, **4**, 757–792.
4 Y. Liang and Y. Yao, *Joule*, 2018, **2**, 1690–1706.
5 Y. Liang, Z. Tao and J. Chen, *Adv. Energy Mater.*, 2012, **2**, 742–769.
6 T. B. Schon, B. T. McAllister, P.-F. Li and D. S. Seferos, *Chem. Soc. Rev.*, 2016, **45**, 6345–6404.
7 P. Poizot, J. Gaubicher, S. Renault, L. Dubois, Y. Liang and Y. Yao, *Chem. Rev.*, 2020, **120**, 6490–6557.
8 Z. Ba, Z. Wang, M. Luo, H. Li, Y. Li, T. Huang, J. Dong, Q. Zhang and X. Zhao, *ACS Appl. Mater. Interfaces*, 2020, **12**, 807–817.
9 M. E. Bhosale, S. Chae, J. M. Kim and J.-Y. Choi, *J. Mater. Chem. A*, 2018, **6**, 19885–19911.
10 Q. Zou, W. Wang, A. Wang, Z. Yu and K. Yuan, *Mater. Lett.*, 2014, **117**, 290–293.
11 W. Du, X. Du, M. Ma, S. Huang, X. Sun and L. Xiong, *Adv. Funct. Mater.*, 2022, **32**, 2110871.
12 T. Janoschka, M. D. Hager and U. S. Schubert, *Adv. Mater.*, 2012, **24**, 6397–6409.
13 K. Nakahara, S. Iwasa, M. Satoh, Y. Morioka, J. Iriyama, M. Suguro and E. Hasegawa, *Chem. Phys. Lett.*, 2002, **359**, 351–354.
14 C. Su, L. Ji, L. Xu, N. Zhou, G. Wang and C. Zhang, *RSC Adv.*, 2016, **6**, 22989–22995.
15 S. E. Burkhardt, S. Conte, G. G. Rodriguez-Calero, M. A. Lowe, H. Qian, W. Zhou, J. Gao, R. G. Hennig and H. D. Abruña, *J. Mater. Chem.*, 2011, **21**, 9553–9563.
16 G. Weng, Y. Su, Z. Liu, J. Zhang, W. Dong and C. Xu, *Energy*, 2009, **34**, 1351–1354.
17 A. H. Gemeay, H. Nishiyama, S. Kuwabata and H. Yoneyama, *J. Electrochem. Soc.*, 1995, **142**, 4190.
18 H. Karami, M. F. Mousavi and M. Shamsipur, *J. Power Sources*, 2003, **124**, 303–308.
19 L. Liu, F. Tian, X. Wang, Z. Yang, M. Zhou and X. Wang, *React. Funct. Polym.*, 2012, **72**, 45–49.
20 D. Yang and Z. Gao, *Synth. Met.*, 2000, **108**, 89–94.
21 H. Yang, S. Zhang, L. Han, Z. Zhang, Z. Xue, J. Gao, Y. Li, C. Huang, Y. Yi, H. Liu and Y. Li, *ACS Appl. Mater. Interfaces*, 2016, **8**, 5366–5375.
22 D.-H. Yang, Z.-Q. Yao, D. Wu, Y.-H. Zhang, Z. Zhou and X.-H. Bu, *J. Mater. Chem. A*, 2016, **4**, 18621–18627.
23 F. Xu, S. Jin, H. Zhong, D. Wu, X. Yang, X. Chen, H. Wei, R. Fu and D. Jiang, *Sci. Rep.*, 2015, **5**, 8225.
24 Y. Liang, P. Zhang and J. Chen, *Chem. Sci.*, 2013, **4**, 1330–1337.
25 Z. Zhu, M. Hong, D. Guo, J. Shi, Z. Tao and J. Chen, *J. Am. Chem. Soc.*, 2014, **136**, 16461–16464.
26 Z. Song, Y. Qian, M. L. Gordin, D. Tang, T. Xu, M. Otani, H. Zhan, H. Zhou and D. Wang, *Angew. Chem., Int. Ed.*, 2015, **54**, 13947–13951.
27 A. Saal, T. Hagemann and U. S. Schubert, *Adv. Energy Mater.*, 2021, **11**, 2001984.
28 Q. Zhang, X. Cui, S. Hao, Q. Zhang, Z. Guo, H. Li, Z. Lin and Y. Yang, *Mater. Today*, 2021, **50**, 170–198.
29 Q. Zhang, Y. Dou, Q. He, S. Deng, Q. Huang, S. Huang and Y. Yang, *Energy Environ. Mater.*, 2022, **5**, 1037–1059.
30 Q. Zhang, G. Lin, Y. He, X. Cui and Y. Yang, *Mater. Today Chem.*, 2020, **17**, 100341.
31 X. Zhang, X. Cui, C.-H. Lu, H. Li, Q. Zhang, C. He and Y. Yang, *Chem. Eng. J.*, 2020, **401**, 126031.
32 Z. Song, H. Zhan and Y. Zhou, *Angew. Chem., Int. Ed.*, 2010, **49**, 8444–8448.
33 G. Hernández, M. Salsamendi, S. M. Morozova, E. I. Lozinskaya, S. Devaraj, Y. S. Vygodskii, A. S. Shaplov and D. Mecerreyes, *J. Polym. Sci., Part A: Polym. Chem.*, 2018, **56**, 714–723.
34 H. Wang, S. Yuan, D. Ma, X. Huang, F. Meng and X. Zhang, *Adv. Energy Mater.*, 2014, **4**, 1301651.
35 P. Sharma, D. Damien, K. Nagarajan, M. M. Shaijumon and M. Hariharan, *J. Phys. Chem. Lett.*, 2013, **4**, 3192–3197.
36 Y. Hu, Y. Gao, L. Fan, Y. Zhang, B. Wang, Z. Qin, J. Zhou and B. Lu, *Adv. Energy Mater.*, 2020, **10**, 2002780.
37 Y. Shi, J. Yang, J. Yang, Z. Wang, Z. Chen and Y. Xu, *Adv. Funct. Mater.*, 2022, **32**, 2111307.
38 H. P. Wu, Q. Yang, Q. H. Meng, A. Ahmad, M. Zhang, L. Y. Zhu, Y. G. Liu and Z. X. Wei, *J. Mater. Chem. A*, 2016, **4**, 2115–2121.
39 Q. Zhang, Y. He, Y. Wang, J. Lu, N. Jiang and Y. Yang, *Adv. Funct. Mater.*, 2023, **33**, 2211590.
40 C. Chen, X. Zhao, H.-B. Li, F. Gan, J. Zhang, J. Dong and Q. Zhang, *Electrochim. Acta*, 2017, **229**, 387–395.
41 T. Le Gall, K. H. Reiman, M. C. Grossel and J. R. Owen, *J. Power Sources*, 2003, **119–121**, 316–320.
42 W. Wei, L. Li, L. Zhang, J. Hong and G. He, *Mater. Lett.*, 2018, **213**, 126–130.
43 C. Li, H. Tan, J. Pei, C. Wang, C. Fan, F. Huang, B. Cao, M. Hao, Y. Li, Z. Wang and J. Li, *New J. Chem.*, 2017, **41**, 14539–14544.
44 F. Xu, J. Xia and W. Shi, *Electrochem. Commun.*, 2015, **60**, 117–120.
45 C. Wang, H. Dong, L. Jiang and W. Hu, *Chem. Soc. Rev.*, 2018, **47**, 422–500.
46 P. Xu, F. Gao and D. Liu, *Adv. Mater. Interfaces*, 2023, **10**, 2300464.
47 G. Wang, N. Chandrasekhar, B. P. Biswal, D. Becker, S. Paasch, E. Brunner, M. Addicoat, M. Yu, R. Berger and X. Feng, *Adv. Mater.*, 2019, **31**, 1901478.
48 Z. Luo, L. Liu, J. Ning, K. Lei, Y. Lu, F. Li and J. Chen, *Angew. Chem., Int. Ed.*, 2018, **57**, 9443–9446.
49 Q. Feng, Y. Cao, C. Guo, L. Chen, W. Sun and Y. Wang, *ACS Appl. Energy Mater.*, 2023, **6**, 7899–7907.
50 Z. Li, J. Zhou, R. Xu, S. Liu, Y. Wang, P. Li, W. Wu and M. Wu, *Chem. Eng. J.*, 2016, **287**, 516–522.

 

51 H. Gao, Q. Zhu, A. R. Neale, M. Bahri, X. Wang, H. Yang, L. Liu, R. Clowes, N. D. Browning, R. S. Sprick, M. A. Little, L. J. Hardwick and A. I. Cooper, *Adv. Energy Mater.*, 2021, **11**, 2101880.
52 L. Yao, C. Ma, L. Sun, D. Zhang, Y. Chen, E. Jin, X. Song, Z. Liang and K.-X. Wang, *J. Am. Chem. Soc.*, 2022, **144**, 23534–23542.
53 Y. Zu, Y. Xu, L. Ma, Q. Kang, H. Yao and J. Hou, *ACS Appl. Mater. Interfaces*, 2020, **12**, 18457–18464.
54 L. Chen, Y. Li, X. Wang, J. Wu, Y. Ding, S.-B. Ren, L. Zhang, Z. Xu, B. Chen, D.-M. Han and Y. Wu, *Chem. Eng. J.*, 2023, **464**, 142658.
55 H. Lyu, P. Li, J. Liu, S. Mahurin, J. Chen, D. K. Hensley, G. M. Veith, Z. Guo, S. Dai and X.-G. Sun, *ChemSusChem*, 2018, **11**, 763–772.
56 S. Zheng, L. Miao, T. Sun, L. Li, T. Ma, J. Bao, Z. Tao and J. Chen, *J. Mater. Chem. A*, 2021, **9**, 2700–2705.
57 K. Lei, F. Li, C. Mu, J. Wang, Q. Zhao, C. Chen and J. Chen, *Energy Environ. Sci.*, 2017, **10**, 552–557.
58 J. Li, M. Luo, Z. Ba, Z. Wang, L. Chen, Y. Li, M. Li, H.-B. Li, J. Dong, X. Zhao and Q. Zhang, *J. Mater. Chem. A*, 2019, **7**, 19112–19119.
59 K. T. Sarang, A. Miranda, H. An, E.-S. Oh, R. Verduzco and J. L. Lutkenhaus, *ACS Appl. Polym. Mater.*, 2019, **1**, 1155–1164.
60 L. Liu, L. Miao, L. Li, F. Li, Y. Lu, Z. Shang and J. Chen, *J. Phys. Chem. Lett.*, 2018, **9**, 3573–3579.